analytical chemistry

pubs.acs.org/ac Article

Advancing Microfluidic Photoelectrochemical Aptasensing Platform with Photogenerated Carrier Regulation for Protein Biosynthesis Inhibitors Detection

Dongquan Leng, Lei Song, Yu Du, Nuo Zhang, Hongmin Ma, Tingting Wu,* Huangxian Ju,* and Qin Wei*

Cite This: *Anal. Chem.* 2025, 97, 17788−17794 Read Online

ACCESS | Metrics & More | Article Recommendations | Supporting Information

ABSTRACT: Regulating the microscale carrier transport in semiconductor materials to enhance the macroscopic photoelectrochemical properties would drive technological advancement and industrial upgrading. In this work, we integrated the maturity of microfluidic technology control methods with current photoelectrochemical analysis sensing techniques to establish a microfluidic photoelectrochemical induction system by modulating the photon-to-current efficiency under zero bias. Traditionally, target recognition has been achieved by affecting the transport of carriers through the space resistance equivalent of the solid−liquid contact interface, which is limited in sensitivity enhancement. In this work, we presented an in situ ion exchange reaction that directly affects $SnO_2/CdLa_2S_4$ semiconductor structure and bandgap matching to achieve accurate detection of the protein biosynthesis inhibitor kanamycin. We developed a microfluidic system to precisely control the flow of the analyte solution, ensuring the controlled delivery of copper ions in proportion to the kanamycin concentration by a hybridization chain reaction within the recognition area. The integration of the microfluidic photoelectrochemical aptasensing platform enhanced the performance of the platform in terms of sensitivity and limits of detection. This work could open up new possibilities for the development of highly efficient and reliable aptasensing systems for various applications in the biomedical and environmental fields.

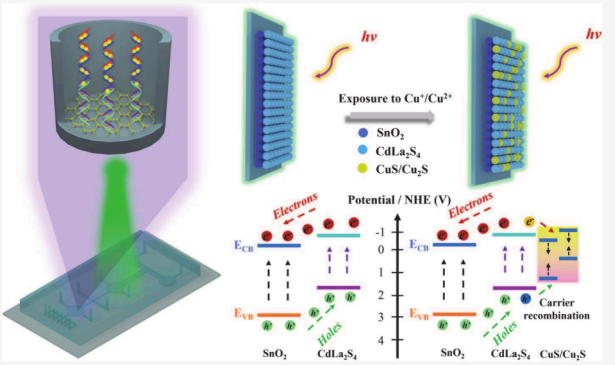

INTRODUCTION

The investigation and development of photoelectrochemical (PEC) biosensors hold a preeminent position within the realm of modern analytical chemistry.[1−3] As an innovative detection technology, PEC biosensors possess high sensitivity, good selectivity, fast response time, easy integration, and strong portability, making them widely applied in environmental monitoring, biomedical research, and food safety.[4−7] Current research efforts are focused on material selection, structural design, and detection strategy principal aspects.[8] The research includes the selection and modification of nanomaterials with high photoelectrochemical efficiency and stability, as well as the design and fabrication of novel PEC biosensors using nanotechnology and molecular modification techniques.[9−11] Therefore, the integrated utilization of modern detection techniques to develop PEC detection strategies with high sensitivity, selectivity, and stability has become the mainstream direction in photoelectrochemical analysis. In recent technological advancements, emerging interdisciplinary microfluidic technology has made significant progress in the design and fabrication of miniaturized systems through deep integration with fluid dynamics, chemistry, microelectronics, advanced material science, biology, and biotechnology.[12−14] This technology offers a groundbreaking platform for sample collection, separation, mixing, and chemical reactions, as well as the implementation of high-sensitivity, high-throughput, and cost-effective analysis, all enabled by its unique functionality.[15−18] Furthermore, through integration and automation, it enables efficient analytical processes while maintaining cost-effective standards.[19,20] Therefore, the integration of microfluidic technology and photoelectrochemical analysis will become a key force in driving the development of analytical science toward precision, efficiency, and cost-effectiveness, demonstrating unlimited potential and broad application prospects in modern scientific research and development.[21−24]

Modulating the microscale carrier transport of semiconductor materials to enhance their macroscopic photoelectrochemical properties is a crucial issue in achieving target

Received: May 30, 2025
Revised: August 2, 2025
Accepted: August 4, 2025
Published: August 9, 2025

https://doi.org/10.1021/acs.analchem.5c03246
Anal. Chem. 2025, 97, 17788−17794

Scheme 1. Microfluidic Chip Fabrication and Kanamycin Detection

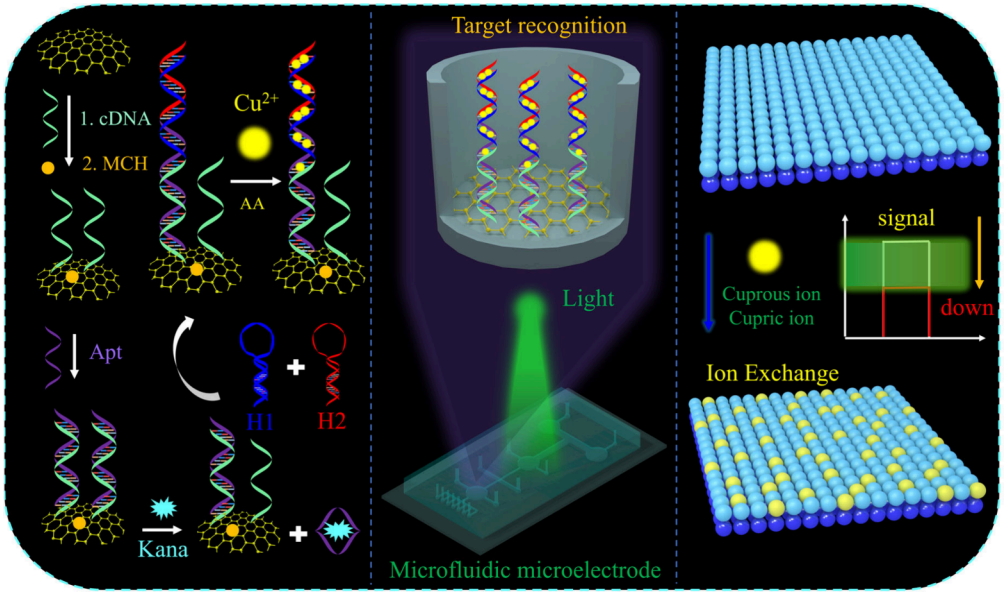

identification during photoelectrochemical analysis.[25−27] Traditionally, target identification is achieved by the spatial resistance effect of the solid−liquid interface, which affects carrier transport. However, this approach has limited sensitivity in improving analysis.[28,29] The ion exchange strategy allows precise control over nanocomposite structures at the atomic or molecular level. This strategy begins by considering the material composition and aligning heterojunction bandgaps. The aim is to alter the potential difference associated with charge separation in the existing heterojunction.[30,31] This method modifies the electronic structure and energy band position of materials, altering the electronic transport pathways within the original ordered microscale structures. It extends the carrier migration distance within the material, thereby enhancing the carrier recombination efficiency.[32,33] This highly sensitive strategy for modulating carrier migration lays a solid foundation for highly sensitive photoelectrochemical bioassays.

In this work, the combination of SnO_2 with good chemical and photostability[34,35] and $CdLa_2S_4$ with excellent visible and near-infrared light absorption properties[36,37] has been used to prepare a $SnO_2/CdLa_2S_4$ heterojunction composite structure with efficient separation of photogenerated charge carriers. A microfluidic system was employed to create a biometric recognition zone and a PEC detection zone. In the biometric recognition zone, the flow of the analyte solution was precisely controlled to ensure the delivery of copper ions in proportion to the kanamycin concentration via hybridization chain reactions. Additionally, ion exchange strategies were implemented to tailor the $SnO_2/CdLa_2S_4$ semiconductor structure and optimize bandgap matching, enabling accurate detection of kanamycin (Kana). Overall, advanced microfluidic control methods were combined with PEC sensing technologies to establish a microfluidic PEC induction system achieved by modulating the photon current efficiency under zero bias conditions.

EXPERIMENTAL SECTION

Experimental Reagents and Methods. The relevant part of the experiment (preparation of materials, reagents, etc.) was placed in Supporting Information.

Procedure of the Microfluidic Microelectrode Preparation. Oil ink protection was selectively applied via screen printing technology to the three-electrode positions on conductive ITO substrates, subsequent to which the specimens were dried for a duration of 10 h at a temperature of 70 °C. Subsequently, wet chemical etching was employed to remove the conductive layer, with the electrodes being completely immersed in an etchant solution ($FeCl_3$: HNO_3: HCl = 0.5 M: 1 M: 1 M) at room temperature for a static retention period of 0.5 h. Following this process, the fabricated electrodes underwent ultrasonic cleaning for 1 h each in acetone, ultrapure water, and anhydrous ethanol. Sequential drop-casting of $SnO_2/CdLa_2S_4$ was performed at the working electrode position, followed by annealing at 200 °C for 2 h in a muffle furnace. Thereafter, the prepared ITO substrates were screen-printed with Ag/AgCl conductive ink at the reference electrode position, followed by drying at 120 °C for a half-hour duration. Furthermore, the carbon paste screen was progressively applied to the electrode positions, which upon drying at 120 °C yielded a three-electrode system precursor for microfluidic electrodes. Then gold nanoparticles were sputtered in the biometric recognition zone by the ion sputtering method. Utilizing the designed drawings in Auto CAD, a microfluidic template and an isolation membrane template were fabricated employing soft lithography techniques, along with polydimethylsiloxane (PDMS)—a curing agent and base agent, in a mass ratio of 1:10. Ultimately, the PDMS-based isolation membrane and the dual-channel microfluidic membrane were adhered to the prepared ITO substrate, thereby obtaining microfluidic chip electrodes. Detailed structural diagrams and physical pictures are included in Figure S1 of Supporting Information.

Microfluidic Chip Fabrication and Detection Procedure. As shown in Scheme 1, on the prepared microfluidic microelectrode platform, complementary chains (2 μM, 10 μL), 6-mercapto-1-hexanol (MCH, 1 mM, 10 μL), aptamer (Apt, 2 μM, 10 μL, corresponding sequence in Table S1), different concentrations of kanamycin, and hairpin DNA after reaction at 95 °C for 5 min (H1 and H2, 5 μM, 10 μL) were injected in sequence at different injection portals. After each

https://doi.org/10.1021/acs.analchem.5c03246
Anal. Chem. 2025, 97, 17788−17794

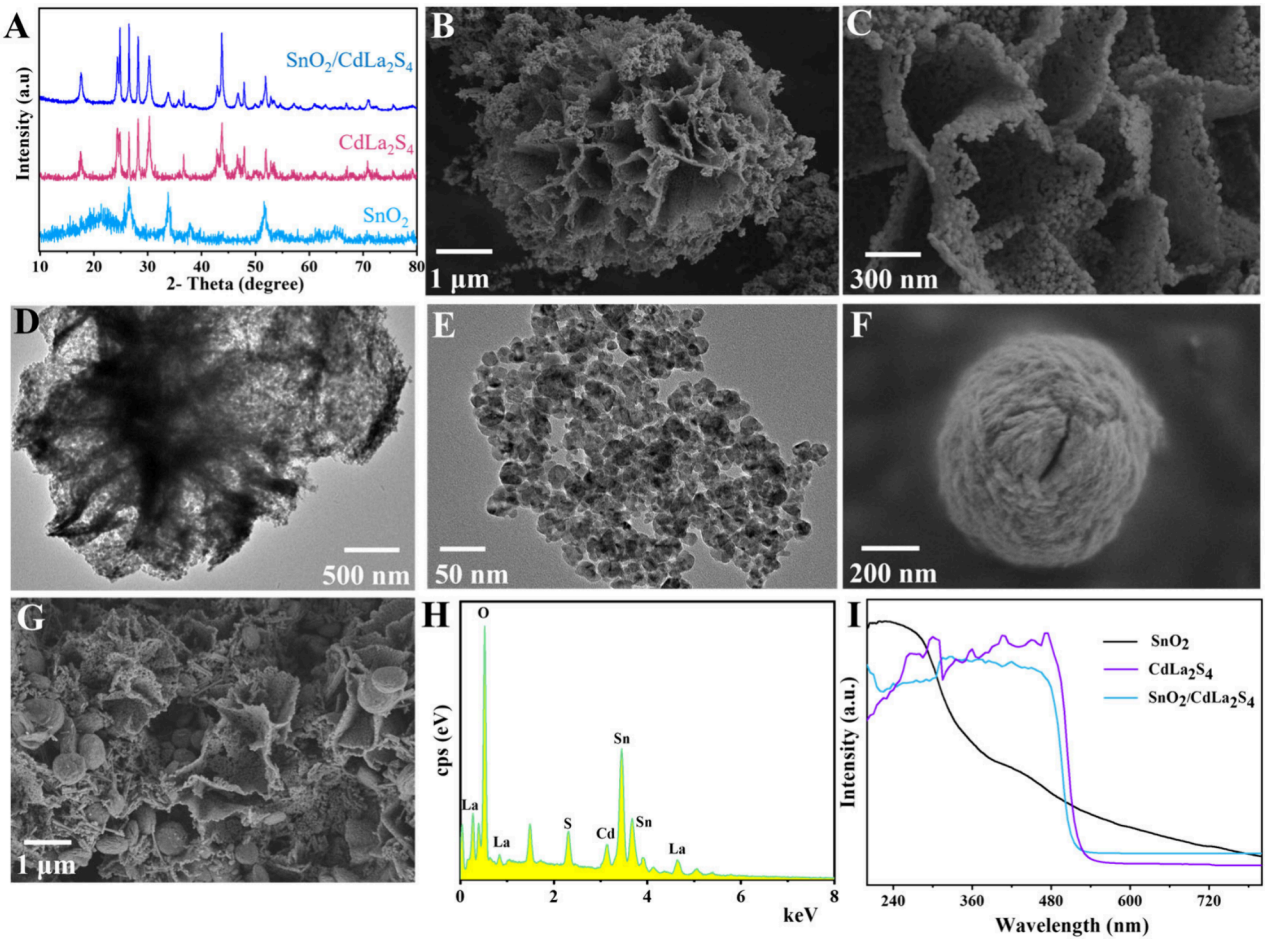

Figure 1. (A) XRD image of SnO_2, $CdLa_2S_4$, and $SnO_2/CdLa_2S_4$, (B) and (C) SEM images of SnO_2, (D) and (E) TEM images of $CdLa_2S_4$, (F) SEM images of $CdLa_2S_4$, (G) SEM images of $SnO_2/CdLa_2S_4$, (H) EDS spectrum of $SnO_2/CdLa_2S_4$, (I) UV−vis spectroscopy image of SnO_2, $CdLa_2S_4$, and $SnO_2/CdLa_2S_4$.

step, the reaction solution was washed and left at room temperature in the reaction zone for 1 h. Then, $CuSO_4$ (500 μM, 10 μL) and ascorbic acid (AA, 500 μM, 10 μL) solutions were added, and the remaining solution was transferred to the PEC detection area after 30 min. In this process, cation exchange of metal ions and PEC materials occurred, and the solution was discharged and washed after 5 min. Finally, after closing the air control switch to separate the target object recognition area from the PEC detection area, the three-electrode area was filled with 0.1 M PBS solution, and the microfluidic chip platform was placed under the LED light source (100 mW/cm^2) for testing.

RESULTS AND DISCUSSION

Characterization of Materials. The material properties and structural characteristics of SnO_2, $CdLa_2S_4$, and the $SnO_2/CdLa_2S_4$ composite heterostructures were investigated by using a combination of analytical techniques. X-ray diffraction (XRD) analysis was employed to determine the crystal structure and phase purity of the samples in Figure 1A. The XRD patterns of SnO_2 and $CdLa_2S_4$ revealed well-defined peaks corresponding to literature data,[36,38] indicating the successful synthesis of SnO_2, $CdLa_2S_4$, and the $SnO_2/CdLa_2S_4$ composite heterostructures. The morphological features of SnO_2, $CdLa_2S_4$, and $SnO_2/CdLa_2S_4$ were examined using scanning electron microscopy (SEM). The SEM images revealed that the SnO_2 nanoflowers consist of lamellar structures in Figure 1B,C. Further structural details were obtained by using transmission electron microscopy (TEM). TEM images of the SnO_2 nanoflowers showed well-defined, flower-like architectures with individual petals composed of fine nanoparticles, which may contribute to enhanced surface area and PEC activity in Figure 1D,E. The $CdLa_2S_4$ nanodisks displayed a uniform disklike shape with the diameter of 600−800 nm (Figure 1F). These observations confirmed the distinct morphologies of the individual components. Conversely, $SnO_2/CdLa_2S_4$ composite materials showed that the nanodisks were chimeric in the flower-like structure, which proved the successful synthesis of the composite materials (Figure 1G). The compositional analysis of the $SnO_2/CdLa_2S_4$ composite was performed using energy dispersive spectroscopy (EDS) mapping in Figure 1H. The EDS results confirmed the presence of Sn, O, Cd, La, and S elements in the composite material. Furthermore, the EDS maps corresponding to $SnO_2/CdLa_2S_4/CuS/Cu_2S$ after ion exchange are presented in Figure S2, which confirms the presence of copper ions or subcopper ions. The optical properties of the materials were investigated by using solid-state ultraviolet−visible (UV−vis) spectroscopy (Figure 1I). The SnO_2 nanoflowers displayed a strong absorption band in the UV region, which can be attributed to the bandgap of SnO_2. The $CdLa_2S_4$ nanodisks showed a broad absorption band extending into the visible region, which

https://doi.org/10.1021/acs.analchem.5c03246
Anal. Chem. 2025, 97, 17788−17794

is characteristic of their semiconductor properties. For the $SnO_2/CdLa_2S_4$ composite material, its UV−vis spectrum indicates that $CdLa_2S_4$ exhibits a good sensitization effect on the wide bandgap SnO_2. The absorption range of visible light covers most of the $CdLa_2S_4$, enabling the composite material to have excellent absorption properties within the visible light range. Comprehensive characterization using XRD, SEM, TEM, EDS, and UV−vis spectroscopy confirmed the successful synthesis of nanoflower-shaped SnO_2, nanodisk-shaped $CdLa_2S_4$, and their composite structure.

X-ray photoelectron spectroscopy (XPS) analysis was conducted to elucidate the surface composition and electronic state of SnO_2 and $CdLa_2S_4$. The XPS spectrum of SnO_2 (Figure 2A) presents distinct peaks corresponding to the Sn

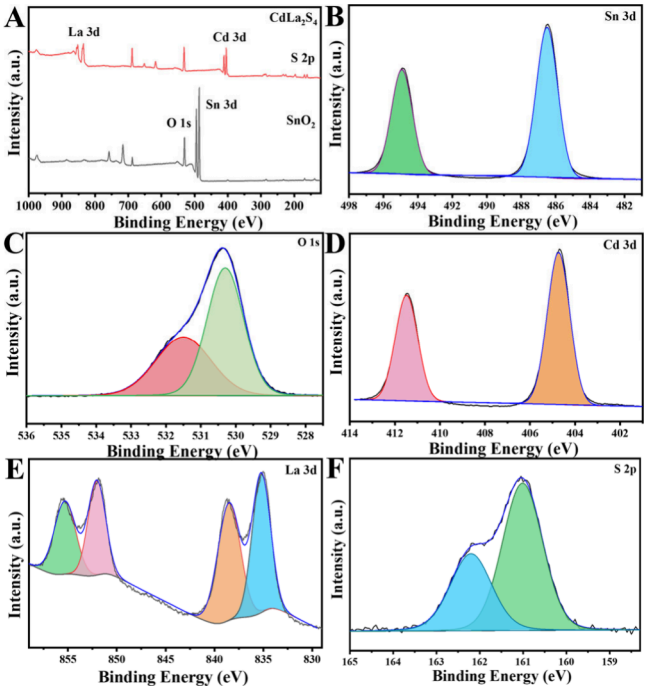

Figure 2. (A) XPS spectra of SnO_2 and $CdLa_2S_4$. XPS high-resolution spectrum of (B) Sn 3d, (C) O 1s, (D) Cd 3d, (E) La 3d, and (F) S 2p.

and the O species. The Sn 3d spectrum (Figure 2B) is deconvoluted into two peaks located at binding energies of 486.4 and 494.9 eV, which are attributed to the Sn $3d_{5/2}$ and Sn $3d_{3/2}$ orbitals, respectively, indicating the presence of Sn in a +4 oxidation state. The O 1s spectrum (Figure 2C) exhibits a peak at a binding energy of 530.3 eV, corresponding to lattice oxygen (O^{2-}) species. Additional peaks at 531.5 eV can be assigned to surface-adsorbed hydroxyl groups (OH^-). The XPS spectrum of $CdLa_2S_4$ (Figure 2A) reveals peaks associated with the Cd, La, and S species. The Cd 3d spectrum (Figure 2D) displays two peaks at binding energies of 404.8 and 411.5 eV, corresponding to the Cd $3d_{5/2}$ and Cd $3d_{3/2}$ orbitals, respectively. These peaks are indicative of Cd in a +2 oxidation state. The La 3d spectrum (Figure 2E) shows peaks at 835.1, 838.8, 852.1, and 855.3 eV, which are characteristic of the La $3d_{5/2}$ and La $3d_{3/2}$ orbitals. Furthermore, the S 2p spectrum (Figure 2F) exhibits two peaks at approximately 161.0 and 162.2 eV corresponding to the S $2p_{3/2}$ and S $2p_{1/2}$ orbitals, suggesting the presence of sulfur in a sulfide form. The XPS data not only confirm the presence of the expected elements in SnO_2 and $CdLa_2S_4$ but also provide insights into the electronic states and chemical environments of these elements within the materials. To further confirm the oxidation state of copper ions in the complex, the total XPS spectra of $SnO_2/CdLa_2S_4$ after ion exchange and the high-resolution Cu 2p spectrum were presented in Figure S3. The characteristic peaks of Cu^+ and Cu^{2+} proved that CuS and Cu_2S were present in the composite material.

Microfluidic Chip Feasibility Analysis and Optimization. In the context of developing highly sensitive and reliable biosensing platforms, the feasibility of our proposed sensor was thoroughly evaluated through photoelectrochemical and electrochemical impedance measurements. The photoelectrochemical performance of the modified $SnO_2/CdLa_2S_4$ photoelectrode was assessed by using PEC tests (I-t curves). Compared with single-electrode materials SnO_2 and $CdLa_2S_4$, a significant increase in the photocurrent was observed after modification (Figure 3A), indicating the successful enhance-

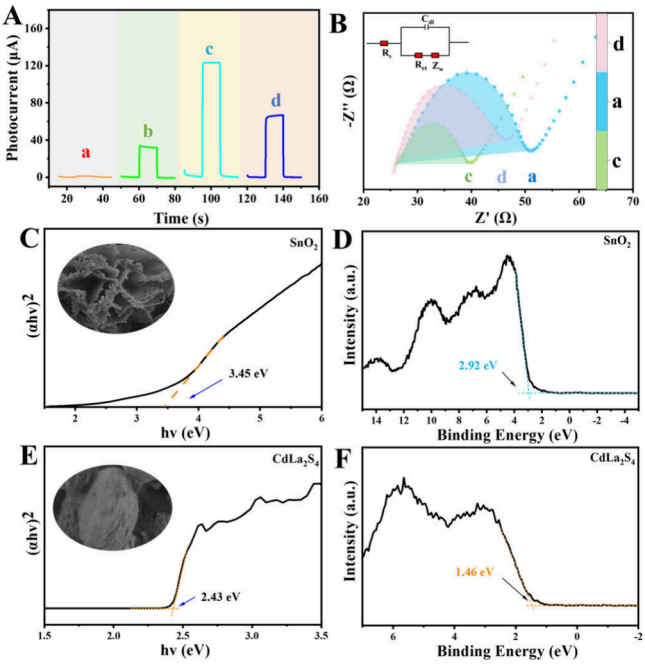

Figure 3. (A) PEC response of (a) ITO/SnO_2, (b) ITO/$CdLa_2S_4$, (c) ITO/SnO_2/$CdLa_2S_4$, and (d) ITO/SnO_2/$CdLa_2S_4$/CuS/Cu_2S in PBS (0.1 M, pH = 7.2) and (B) EIS in 5.0 mM $[Fe(CN)_6]^{3-/4-}$containing 0.1 M KCl, Tauc plots of SnO_2 (C), XPS valence band spectra of SnO_2 (D), Tauc plots of $CdLa_2S_4$ (E), and XPS valence band spectra of $CdLa_2S_4$ (F).

ment of the light absorption and charge separation capabilities. However, the introduction of copper ions leads to the weakening of the photocurrent, which proves that the ion exchange reaction can reduce the performance of the photoelectrode. Electrochemical impedance spectroscopy (EIS) was employed to further evaluate the charge transfer properties of the modified sensor (Figure 3B). The EIS measurements revealed a decrease in the charge transfer resistance of the $SnO_2/CdLa_2S_4$ photoelectrode, indicating an improvement in the electron transfer rate at the solid−liquid interface. The introduction of copper ions creates a blocking layer at the semiconductor-electrolyte interface, impeding the flow of electrons and increasing the resistance. The results

https://doi.org/10.1021/acs.analchem.5c03246
Anal. Chem. 2025, 97, 17788−17794

obtained from these experiments provide compelling evidence for the viability of the sensor design.

To achieve the optimal performance of microfluidic sensor chips, we systematically investigated and adjusted key experimental parameters such as buffer solution composition and incubation time. The influence of the buffer solution on the sensor performance was evaluated by testing different pH levels. We found that PBS at pH 7.2 provided the most stable and sensitive response for the detection of kanamycin (Figure S5A). This buffer was chosen for subsequent experiments. And we examined the effect of incubation time on the sensor response by varying the time allowed for copper ions with the nucleic acid strand. The optimal incubation time was found to be 30 min, which provided the highest PEC response for kanamycin detection (Figure S5B).

Possible Mechanisms of PEC Response. The photoelectrochemical response of the $SnO_2/CdLa_2S_4$ semiconductor material was investigated as a crucial aspect of the microfluidic photoelectrochemical system. The PEC performance is attributed to several factors, including the bandgap of materials, carrier dynamics, and the modification of its surface properties upon copper ion exchange. Here, we discuss the possible mechanisms contributing to the observed PEC response. The Tauc plots and XPS valence band spectra were used to calculate the band gap (E_g) and valence band (E_{VB}) of the material, and then the conduction band (E_{CB}) was calculated based on $E_{VB} = E_g + E_{CB}$. First, the SnO_2, $CdLa_2S_4$, and $SnO_2/CdLa_2S_4$ materials exhibit a suitable bandgap (Scheme 2a) for the absorption of visible light (SnO_2: E_g = 3.45 eV (Figure 3C), E_{VB} = 3.28 eV (Figure 3D), E_{CB} = −0.17 eV; $CdLa_2S_4$: E_g = 2.43 eV (Figure 3E), E_{VB} = 1.82 eV (Figure 3F), E_{CB} = −0.61 eV, $SnO_2/CdLa_2S_4$: E_g = 2.45 eV (Figure S4A), E_{VB} = 1.84 eV (Figure S4D), E_{CB} = −0.61 eV, φ=4.8 eV), which enables efficient conversion of photon energy into electrical energy. Upon illumination, the photogenerated electrons and holes are separated, leading to the generation of a photoelectric signal. The following mechanisms are proposed to explain the PEC response: The incorporation of $CdLa_2S_4$ into SnO_2 increases the interface area between the two materials, leading to enhanced charge separation and reduced recombination rates. And the $SnO_2/CdLa_2S_4$ composite structure facilitates efficient charge transport due to the shorter diffusion length of carriers and the increased number of charge transport channels. This results in a higher photocurrent and improved PEC performance under zero bias. This enhances the macroscopic photoelectrochemical properties of the material. Then the microfluidic system enables the precise delivery of copper ions, which correspond to the concentration of kanamycin in the analyte solution. The in situ ion exchange reaction between copper ions and cadmium ions in the $SnO_2/CdLa_2S_4$ material alters the bandgap structure of semiconductors, leading to a decrease in the photogenerated electron−hole pairs. And the introduction of copper ions results in the formation of CuS and Cu_2S with narrow bandgap (CuS: E_g = 1.52 eV (Figure S4B), E_{VB} = 1.29 eV (Figure S4E), E_{CB} = −0.23 eV; Cu_2S: E_g = 1.47 eV (Figure S4C), E_{VB} = 0.78 eV (Figure S4F), E_{CB} = −0.69 eV), which allows for the formation of electron hole recombination centers and further quenching the PEC performance (Scheme 2b). This analyte-specific ion exchange reaction serves as a highly sensitive detection mechanism for protein biosynthesis inhibitor kanamycin.

Scheme 2. Mechanism of PEC Signal of Photoelectrode

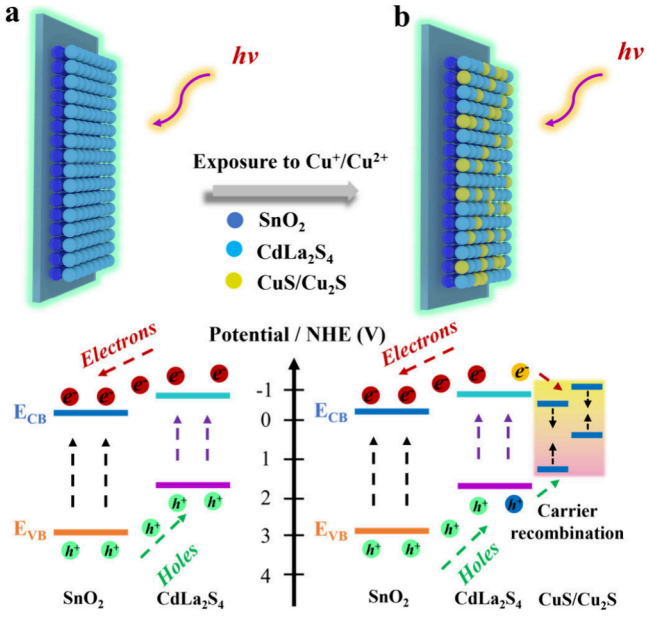

Kanamycin Analysis. Kanamycin, an antibiotic commonly used for the treatment of various bacterial infections, requires precise monitoring due to its potential for nephrotoxicity and ototoxicity. The microfluidic sensor chips were utilized to analyze a range of kanamycin concentrations (0.02 pg/mL - 100 ng/mL) outlined in Figure 4A under the optimized experimental conditions. This relationship was utilized to construct a calibration curve (Figure 4B), which demonstrated a strong linear correlation between the PEC signal and the logarithm of the kanamycin concentration. The calibration curve was described by the equation $I = 47.88 - 11.90 \lg c$ (ng/mL), where I represents the PEC signal and c is the concentration of kanamycin. The high correlation coefficient (R^2 = 0.991) indicated the reliability and accuracy of the sensor response. And the detection limit of the sensor was determined to be 12 fg/mL. The sensitivity and detection limit of our sensor were comparable to or even superior to those

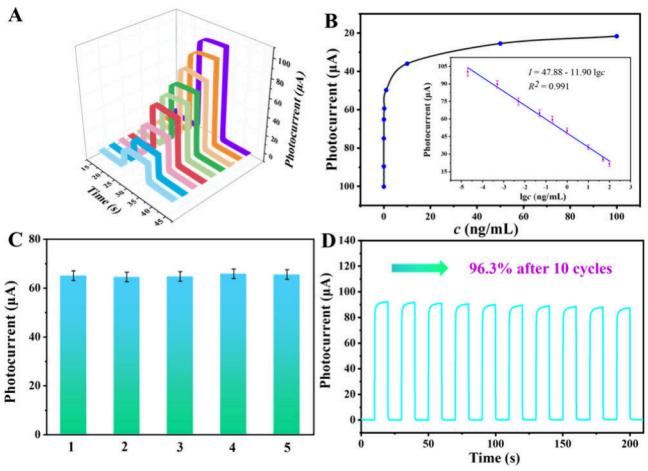

Figure 4. (A) Photocurrent response and (B) the corresponding calibration curve of kanamycin detection in PBS (0.1 M, pH = 7.2), (C) reproducibility test (c = 0.05 ng/mL), (D) stability test (c = 0.5 pg/mL). Error bars are SD (n = 3).

https://doi.org/10.1021/acs.analchem.5c03246
Anal. Chem. 2025, 97, 17788−17794

reported in the existing literature (Table S2), highlighting its potential for practical application.

Performance Analysis of Microfluidic Chip. The performance of a biosensor is critically assessed based on its reproducibility, stability, and selectivity. To assess the reproducibility of the biosensor, we conducted independent measurements using different batches of the sensor (Figure 4C). The reproducibility tests yielded an RSD of 3.5%, which is within an acceptable range for biosensor applications. The stability of the biosensor was evaluated by measuring the PEC signal over multiple consecutive cycles (Figure 4D). The sensor was subjected to repeated measurements of kanamycin at a concentration of 0.5 pg/mL. After ten consecutive on and off light tests, the PEC signal remained within 96.3%, and the biosensor showed excellent stability. In addition, we selected chloramphenicol (CAP), ciprofloxacin (CIP), erythromycin (EM), and tetracycline (TC) as potential interferents due to their common use in clinical settings. The selectivity data, presented in Figure S6, clearly demonstrate the biosensor's ability to distinguish kanamycin from other antibiotics, confirming its specificity for the target analyte. The current reusability of microfluidic platforms is challenged by multiple factors, including aptamer stability, channel integrity, and the cleaning process of PEC materials. Future research will focus on developing effective regeneration methods and improving platform design to enhance its durability and cost-effectiveness in practical applications.

Milk Sample Analysis. To assess the practical utility of our aptasensor for the detection of kanamycin in milk samples, a standard addition method was employed for the quantitative measurement of kanamycin. This method involves spiking known concentrations of kanamycin into unadulterated milk samples to simulate real-world scenarios, where trace amounts of antibiotics might be present. The following concentrations of kanamycin were used in the analysis: 0.10 ng/mL, 1.00 ng/mL, and 5.00 ng/mL. The results of the analysis are presented in Table S3. The recovery rates of kanamycin in the milk samples ranged from 96.0% to 102%, with relative standard deviations below 4.1%. These recovery rates indicate that the aptasensor can accurately quantify kanamycin in milk with minimal variation, suggesting a high precision in the measurements.

CONCLUSION

In summary, this work demonstrates the potential of the microfluidic photoelectrochemical aptasensing platform for a wide range of applications in environmental fields. The favorable bandgap properties and charge transport characteristics of the $SnO_2/CdLa_2S_4$ composite material enhanced the macroscopic photoelectrochemical properties of the system. By optimizing the in situ ion exchange reaction and modulating the photon-to-current efficiency under zero bias, we were able to directly affect the $SnO_2/CdLa_2S_4$ semiconductor structure and bandgap matching, resulting in accurate and sensitive detection of kanamycin. The precise control of analyte flow and delivery of copper ions through the microfluidic system, along with the analyte-specific ion exchange reaction, contributed to the high sensitivity of the platform. The findings of this study contribute to the development of highly efficient and reliable aptasensing systems, which could play a significant role in the advancement of diagnostic and analytical technologies. Future research could focus on extending the capabilities of this platform to detect other target analytes and optimizing the system for practical applications.

ASSOCIATED CONTENT

Supporting Information

The Supporting Information is available free of charge at https://pubs.acs.org/doi/10.1021/acs.analchem.5c03246.

Materials and reagents, apparatus, detailed structural diagrams and physical pictures of microfluidic chip, band gap diagram of SnO_2 and $CdLa_2S_4$, optimization of experimental conditions and other information (PDF)

AUTHOR INFORMATION

Corresponding Authors

Tingting Wu − *Key Laboratory of Interfacial Reaction & Sensing Analysis in Universities of Shandong, School of Chemistry and Chemical Engineering, University of Jinan, Jinan 250022, P. R. China*; Email: wuting7692@163.com

Huangxian Ju − *Key Laboratory of Interfacial Reaction & Sensing Analysis in Universities of Shandong, School of Chemistry and Chemical Engineering, University of Jinan, Jinan 250022, P. R. China*; orcid.org/0000-0002-6741-5302; Email: hxju@nju.edu.cn

Qin Wei − *Key Laboratory of Interfacial Reaction & Sensing Analysis in Universities of Shandong, School of Chemistry and Chemical Engineering, University of Jinan, Jinan 250022, P. R. China; Department of Chemistry, Sungkyunkwan University, Suwon 16419, Republic of Korea*; orcid.org/0000-0002-3034-8046; Email: sdjndxwq@163.com

Authors

Dongquan Leng − *Key Laboratory of Interfacial Reaction & Sensing Analysis in Universities of Shandong, School of Chemistry and Chemical Engineering, University of Jinan, Jinan 250022, P. R. China*

Lei Song − *Key Laboratory of Interfacial Reaction & Sensing Analysis in Universities of Shandong, School of Chemistry and Chemical Engineering, University of Jinan, Jinan 250022, P. R. China*

Yu Du − *School of Water Conservancy and Environment, University of Jinan, Jinan 250022, China*; orcid.org/0000-0002-9002-8845

Nuo Zhang − *Key Laboratory of Interfacial Reaction & Sensing Analysis in Universities of Shandong, School of Chemistry and Chemical Engineering, University of Jinan, Jinan 250022, P. R. China*

Hongmin Ma − *Key Laboratory of Interfacial Reaction & Sensing Analysis in Universities of Shandong, School of Chemistry and Chemical Engineering, University of Jinan, Jinan 250022, P. R. China*; orcid.org/0000-0002-7061-8944

Complete contact information is available at: https://pubs.acs.org/10.1021/acs.analchem.5c03246

Notes

The authors declare no competing financial interest.

ACKNOWLEDGMENTS

This study was supported by the National Natural Science Foundation of China (Nos. 22274062, 22206056), the Natural Science Foundation of Shandong Province (ZR2022QB117,

ZR2024QB058), Postdoctoral Fellowship Program of CPSF (GZC20230957), China Postdoctoral Science Foundation (2023M741360), and Young Talent of Lifting engineering for Science and Technology in Shandong. The authors thank Shiyanjia Lab (www.shiyanjia.com) for XPS analysis.

REFERENCES

(1) Li, Z.; Wang, Z.; Li, J.; Zhu, Q.; Wang, Z.; Dai, Z. *J. Am. Chem. Soc.* **2021**, *143* (34), 13478−13482.
(2) Xu, X.; Xu, D.; Lu, S.; Zhou, X.; Yang, S.; Zhang, Z. *Nat. Commun.* **2024**, *15* (1), 8827.
(3) Ye, X.; Wang, X.; Kong, Y.; Dai, M.; Han, D.; Liu, Z. *Angew. Chem., Int. Ed.* **2021**, *60* (21), 11774−11778.
(4) Chen, F.-Z.; Hou, L.; Gao, Y.; Zhou, J.-Y.; Kong, F.-Y.; Han, D.-M.; Zhao, W.-W. *Adv. Funct. Mater.* **2024**, *34* (48), No. 2408186.
(5) Ding, K.; Zhang, H.; Jiang, J.; Luo, J.; Wu, R.; Ye, L.; Tang, Y.; Pang, D.; Li, H.; Li, W. *Adv. Sci.* **2024**, *11* (43), No. 2407822.
(6) Wang, C.; Wang, Y.; Kirlikovali, K. O.; Ma, K.; Zhou, Y.; Li, P.; Farha, O. K. *Adv. Mater.* **2022**, *34* (35), No. 2202287.
(7) Zhan, W.-w.; Kuang, Q.; Zhou, J.-z.; Kong, X.-j.; Xie, Z.-x.; Zheng, L.-s. *J. Am. Chem. Soc.* **2013**, *135* (5), 1926−1933.
(8) Zhang, H.; Zhou, Y.; Zhang, M.; Cao, Y.; Yin, H.; Ai, S. *Adv. Funct. Mater.* **2024**, *34* (52), No. 2411008.
(9) Liu, L.; Yao, Q.; Jiang, F.; Cai, Z.; Meng, M.; Sun, H.; Zhang, L.; Gong, J. *Anal. Chem.* **2024**, *96* (7), 2939−2948.
(10) Xiao, H.-J.; Wu, P.; Hu, X.-B.; Wang, Y.-L.; Ren, S.-W.; Liu, Y.-M.; Cao, J.-T. *ACS Appl. Mater. Interfaces* **2024**, *16* (12), 14626−14632.
(11) Zhang, M.; Zhou, Y.; Zhang, H.; Yin, H.; Duan, J.; Ai, S. *Anal. Chem.* **2024**, *96* (40), 16080−16090.
(12) Nunes, J. K.; Stone, H. A. *Chem. Rev.* **2022**, *122* (7), 6919−6920.
(13) Paratore, F.; Bacheva, V.; Bercovici, M.; Kaigala, G. V. *Nat. Rev. Chem.* **2022**, *6* (1), 70−80.
(14) Shang, L.; Cheng, Y.; Zhao, Y. *Chem. Rev.* **2017**, *117* (12), 7964−8040.
(15) Goyette, P.-A.; Boulais, É.; Normandeau, F.; Laberge, G.; Juncker, D.; Gervais, T. *Nat. Commun.* **2019**, *10* (1), 1781.
(16) Li, J.; Zheng, Y.; Qiu, J.; Niu, W.; Wu, J.; Cui, H.; Zi, Y.; Li, X. *Nano Energy* **2024**, *119*, No. 109061.
(17) Xie, Y.; Rufo, J.; Zhong, R.; Rich, J.; Li, P.; Leong, K. W.; Huang, T. J. *ACS Nano* **2020**, *14* (12), 16220−16240.
(18) Zhao, Z.; Wang, Z.; Li, G.; Cai, Z.; Wu, J.; Wang, L.; Deng, L.; Cai, M.; Cui, W. *Adv. Funct. Mater.* **2021**, *31* (31), No. 2170227.
(19) Spatola Rossi, C.; Coulon, F.; Ma, S.; Zhang, Y. S.; Yang, Z. *Adv. Funct. Mater.* **2023**, *33* (21), No. 2212081.
(20) Xiong, Q.; Lim, C. Y.; Ren, J.; Zhou, J.; Pu, K.; Chan-Park, M. B.; Mao, H.; Lam, Y. C.; Duan, H. *Nat. Commun.* **2018**, *9* (1), 1743.
(21) Fattahi, Z.; Hasanzadeh, M. *TrAC Trends in Analytical Chemistry* **2022**, *152*, No. 116637.
(22) Feng, J.; Wu, T.; Cheng, Q.; Ma, H.; Ren, X.; Wang, X.; Lee, J. Y.; Wei, Q.; Ju, H. *Lab Chip* **2021**, *21* (2), 378−384.
(23) Li, J.; Yang, Y.; Peng, Z.; Yang, J.; Li, Y. *Biosens. Bioelectron.* **2022**, *217*, No. 114719.
(24) Wu, T.; Du, Y.; Dai, L.; Li, J.; Song, X.; Feng, J.; Wang, X.; Wei, Q.; Ju, H. *Anal. Chem.* **2022**, *94* (30), 10651−10658.
(25) Ghosh, R.; Singh, M.; Chang, L. W.; Lin, H.-I.; Chen, Y. S.; Muthu, J.; Papnai, B.; Kang, Y. S.; Liao, Y.-M.; Bera, K. P.; et al. *ACS Nano* **2022**, *16* (4), 5743−5751.
(26) Rettie, A. J. E.; Lee, H. C.; Marshall, L. G.; Lin, J.-F.; Capan, C.; Lindemuth, J.; McCloy, J. S.; Zhou, J.; Bard, A. J.; Mullins, C. B. *J. Am. Chem. Soc.* **2013**, *135* (30), 11389−11396.
(27) Xiao, Y.; Fan, Z.; Nakabayashi, M.; Li, Q.; Zhou, L.; Wang, Q.; Li, C.; Shibata, N.; Domen, K.; Li, Y. *Nat. Commun.* **2022**, *13* (1), 7769.
(28) Chen, Y.; Zhou, Y.; Yin, H.; Li, F.; Li, H.; Guo, R.; Han, Y.; Ai, S. *Sensor. Actuat. B: Chem.* **2020**, *307*, No. 127633.
(29) Fan, D.; Wang, H.; Khan, M. S.; Bao, C.; Wang, H.; Wu, D.; Wei, Q.; Du, B. *Biosens. Bioelectron.* **2017**, *97*, 253−259.
(30) Leng, D.; Zhao, J.; Ren, X.; Xu, R.; Liu, L.; Liu, X.; Li, Y.; Wei, Q. *Anal. Chem.* **2021**, *93* (30), 10712−10718.
(31) Song, W.; Zhang, F.; Song, P.; Zhang, Z.; He, P.; Li, Y.; Zhang, X. *Sensor. Actuat. B: Chem.* **2021**, *327*, No. 128900.
(32) Wang, L.; Han, J.; Wu, Y.; Zhang, Y.; Zhang, Q.; Tan, X.; Yang, Y.; Li, W.; Bu, Y.; Ao, J.-P. *Chemical Engineering Journal* **2019**, *368*, 710−718.
(33) Zhou, Y.; Lv, S.; Wang, X.-y.; Kong, L.; Bi, S. *Anal. Chem.* **2022**, *94* (41), 14492−14501.
(34) Han, H.; Kment, S.; Karlicky, F.; Wang, L.; Naldoni, A.; Schmuki, P.; Zboril, R. *Small* **2018**, *14* (19), No. 1703860.
(35) Pan, Q.; Li, A.; Zhang, Y.; Yang, Y.; Cheng, C. *Adv. Sci.* **2020**, *7* (3), No. 1902235.
(36) Cheng, L.; Chen, Q.; Li, J.; Liu, H. *Appl. Catal. B: Environ.* **2020**, *267*, No. 118379.
(37) Zhang, H.; Sun, B.; Wang, J.; Zhu, Q.; Hou, D.; Li, C.; Qiao, X.-q.; Li, D.-s. *J. Colloid Interface Sci.* **2023**, *645*, 429−438.
(38) Jiang, L.-Y.; Hu, R.; Wang, A.-J.; Mei, L.-P.; Feng, J.-J. *Sensor. Actuat. B: Chem.* **2023**, *382*, No. 133491.

https://doi.org/10.1021/acs.analchem.5c03246
Anal. Chem. 2025, 97, 17788−17794